Optical Materials 143 (2023) 114248

Contents lists available at ScienceDirect

Optical Materials

journal homepage: www.elsevier.com/locate/optmat

Research Article

Novel $ZnCo_2O_4/WO_3$ nanocomposite as the counter electrode for dye-sensitized solar cells (DSSCs): study of electrocatalytic activity and charge transfer properties

Raed H. Althomali [a], Ebraheem Abdu Musad Saleh [a], Ramesh S. Bhat [b,*], Shavan Askar [c], I.B. Sapaev [d,e,f], Mazin A.A. Najm [g], Benien M. Ridha [h], Ali H. Alsalamy [i], Russual Riyadh [j]

[a] Department of Chemistry, Prince Sattam Bin Abdulaziz University,College of Arts and Science, Wadi Al-Dawasir 11991, Saudi Arabia
[b] Department of Chemistry, NMAM Institute of Technology, Nitte, 574110, Karnataka, India
[c] Erbil Polytechnic University, Erbil Technical Engineering College, Erbil, Iraq
[d] New Uzbekistan University, Tashkent, Uzbekistan
[e] School of Engineering, Central Asian University, Tashkent 111221, Uzbekistan
[f] Tashkent Institute of Irrigation and Agricultural Mechanization Engineers, National Research University, Tashkent, Uzbekistan
[g] Pharmaceutical Chemistry Department, College of Pharmacy, Al-Ayen University, Thi-Qar, Iraq
[h] College of Technical Engineering, The Islamic University, Najaf, Iraq
[i] College of Technical Engineering, Imam Ja'afar Al-Sadiq University, Al-Muthanna 66002, Iraq
[j] Medical Technical College, Al-Farahidi University, Baghdad, Iraq

A R T I C L E I N F O

Keywords:
$ZnCo_2O_4/WO_3$
DSSC
Counter electrode
Electrocatalytic activity

A B S T R A C T

Nowadays, Pt coated FTO is used conventionally as the counter electrode in dye-sensitized solar cell (DSSC). In addition to the high price of the Pt electrode, it reduces the stability of the DSSC. In this study, we introduce and study a new counter electrode based on the $ZnCo_2O_4/WO_3$ composite that is used in DSSC. We show that the efficiency of the DSSC can be enhanced even more then the Pt-based one by employing the $ZnCo_2O_4/WO_3$ as counter electrode. By examining the structural, morphological, optical, and electrochemical properties of the synthesized electrodes, we investigate the counter electrodes synthesized under different conditions. The XRD patterns and FESEM images confirm that the composite phase of the $ZnCo_2O_4/WO_3$ layers is formed. Additionally, electrochemical studies by CV, Tafel, EIS, and Mott-Schottky methods indicate the electrocatalytic activity of the $ZnCo_2O_4/WO_3$ sample have significantly increased compared to $ZnCo_2O_4$ and WO_3 electrodes. Furthermore, the characterization of DSSCs with TiO_2 photoanode and different counter electrodes show that the efficiency of the solar cells based on $ZnCo_2O_4/WO_3$ has a promising efficiency of 7.76%, which has increased by 7% compared to the Pt one.

1. Introduction

Since the introduction of dye-sensitized solar cells (DSSCs) in 1991 by O'Regan and Gratzel [1], they have emerged as a potential alternative for thin-film solar cells. DSSCs have always been affordable due to their low manufacturing cost and non-toxicity, and have also attracted the consideration of environmentalists [2,3]. A typical DSSC consists of photoanode, counter electrode, electrolyte, and adsorptive dye molecules. In the last two decades, extensive research has been carried out on different parts of the DSSC. Investigating the possible structures for the photoanode and using different materials has been studied frequently [4,5]. Widespread studies have been done to replace conventional electrolytes such as I^-/I_3^- and Co^{3+}/Co^{2+} [6,7]. Also, many researchers have sought to find metal coordination complex or organic dye molecules instead of the conventional N719 [8,9]. However, in most cases, non-toxic and inexpensive TiO_2 as photoanode and N719, which has appropriate molecular level aligning with TiO_2, have been the best option. Likewise, due to the proper compatibility of the redox levels of the I^-/I_3^- electrolyte with N719, their joint use is not far from expectation.

In recent years, replacing Pt as the counter electrode and getting rid of this expensive material has attracted the attention of studies [10–14]. The use of materials such as carbon black, graphene-based and

* Corresponding author.
E-mail addresses: rameshbhat@nitte.edu.in (R.S. Bhat), sapaevibrokhim@gmail.com, mohim@inbox.ru (I.B. Sapaev).

https://doi.org/10.1016/j.optmat.2023.114248
Received 15 June 2023; Received in revised form 9 August 2023; Accepted 10 August 2023
Available online 27 August 2023

carbon-based nanoparticles, PEDOT and even some conductive polymers such as PANI has raised hopes for replacing Pt. Narudin et al. [15], by using carbon black-graphite counter electrode enhance the efficiency of DSSC up to 5.74%. Kasi Reddy et al. [16], demonstrate the high electrocatalytic activity of bilayer PEDOT:PSS/SWCNH counter electrodes for achieving 5.1% power to current efficiency. Employing PANI counter electrodes, Karakuş et al. [17], succeeded to attain 6.3% efficiency for standard liquid electrolyte based DSSCs.

Using composite materials and taking advantage of the simultaneous properties of each component can be inspiring. Composite structures can be effective as they have demonstrated before [18]. Gao et al. [19], achieved 8.72% efficiency by synthesizing In_4SnS_8@MoS_2@CNTs composite through hydrothermal method and using it as counter electrode. By replacing the standard Pt counter electrode with PANI/WSe_2 composite one, Sheela et al. [20], attained an 8.22% power to current efficiency, which was higher than that of the pure PANI and WSe_2 or even Pt counter electrodes. Yang et al. [13], elevated the electrocatalytic activity of CZTS counter electrodes by covering Co_9S_8 on CZTS thin film prepared by the spin-coating method. This composite counter electrode demonstrated an improved efficiency of 6.41% in comparison with 3.92% efficiency of bare CZTS counter electrode. Nitrogen-decorated CeO_2/reduced graphene oxide nanocomposite (CeO_2/N-rGO) used as counter electrode in DSSC structure and the electrocatalytic activity for triiodide/iodide reduction been investigated by Wei et al., [21]. The DSSC fabricated based on CeO_2/N-rGO demonstrated an advanced efficiency of 3.20%.

$ZnCo_2O_4$ as an intrinsic p-type material benefits from high conductivity, structural stability, and high electrocatalytic activity [22]. It shows superior electrical conductivity and electrochemical activity than ZnO and Co_3O_4 [23,24]. Meanwhile, it has low manufacturing price due to inexpensive and earth-abundant components, which guarantees the reduced cost-effective production [25]. By environmental friendliness, high electrochemical activity and conductivity, $ZnCo_2O_4$ can be a proper candidate as counter electrode in DSSCs. Also, WO_3 with unique optical and electrochemical properties is another candidate for appropriate reduction of electrolyte species [26]. It also includes good physico-chemical and electrical properties, which can help to improve the electrocatalytic activity of the counter electrode along with the $ZnCo_2O_4$ [27].

$ZnCo_2O_4$ and WO_3 nanostructures have previously been used in DSSC structure as the counter electrode. Hou et al. [28] synthesized flower-like $ZnCo_2O_4$ and graphene oxide nanostructures using solvothermal and common Hummers technique, respectively, and fabricated $ZnCo_2O_4$/RGO nanohybrids as counter electrode using hydrothermal method. Their DSSC based on this hybrid counter electrode has shown an efficiency of 7.22%. Wang et al. [29] have also achieved 6.73% efficiency for DSSC using $ZnCo_2O_4$/RGO composite as the counter electrode. Abdullaev et al. [30] have succeeded in producing core-shell ZnO@$ZnCo_2O_4$ nanostructures that yielded 8.39% efficiency for a DSSC based on this counter electrode. By synthesizing $ZnCo_2O_4$@$NiMoO_4$ composite on carbon paper (CP) by two-step hydrothermal method, Zhang et al. [31] have succeeded in achieving 9.30% efficiency for DSSC with this counter electrode. ZnO@WO_3 core-shell nanoparticles were prepared by Mahajan et al. [32] by sol-gel method, which yielded 5.73% efficiency for DSSC based on this counter electrode. Sulfurization treatment of mesoporous WO_3/carbon film coated on fluorine-doped tin oxide (FTO) glass yielded WO_3@WS_2@-carbon CE by Shen et al. [33]. Photovoltaic performance measurements have showed that the DSSC with the WO_3@WS_2@carbon core-shell counter electrode attained a power conversion efficiency of 7.71%. Tungsten trioxide was sprayed onto ITO conductive glass and filled with activated charcoal powder (ACP) for use as counter electrode in DSSC by Cui et al. [34]. The power conversion efficiency of WO_3@ACP-based DSSC was 5.04%, which has been 3.15 times better than the 1.61% of WO_3 DSSC.

In this research, by preparing a composite layer of $ZnCo_2O_4$ (ZCO) and WO_3 materials and using it as the counter electrode in DSSC, we investigate its properties. WO_3 structures can play an effective role in electron transport due to their proper conductivity. Simultaneously, ZCO nanoparticles can improve the performance of the counter electrode in combination with WO_3 due to their proper electrocatalytic activity and charge transfer properties.

2. Experimental methods

2.1. Synthesis of nanoparticles

A simple and rapid combustion method is used for the synthesis of ZCO nanoparticles. Primary, 1 g $Zn(NO_3)_2 \cdot 6H_2O$ and 2 g $Co(NO_3)_2 \cdot 6H_2O$ were dissolved in 8 g double distilled water, and while stirring vigorously, its temperature raised to 85 °C. Then, 6.5 g $C_6H_8O_7$ was added to the solution and the stirring continued for 15 min. The solution was transferred to an oven to heat at 300 °C for 20 min. After drying, the resulting powder was crushed in a mortar and then annealed for 5 h at a temperature of 600 °C with 5 °C/min rate in air furnace to obtain ZCO nanoparticles.

To synthesize the WO_3 nanostructure, sol-gel method was used. 1.5 g sodium tungstate dihydrate ($Na_2WO_4 \cdot 2H_2O$) were dissolved in 100 ml double distilled water and stirred for 10 min. Then, using 2 M HCl acid, the pH of the solution was reduced to 1.5. This solution was stirred for 11 h at room temperature to obtain a cloudy precipitate of WO_3. The sediments were centrifuged several times and dried at 90 °C for 2 h. To improve the crystallinity, heat treatment was performed on the obtained powders at a temperature of 500 °C for 2 h.

To fabricate the ZCO/WO_3 composite material, solid state reaction method was used to react together the materials we synthesized in the previous steps. ZCO and WO_3 nanostructures with ratio of ZCO:WO_3 = 2:1were transferred into zirconium cups and milled in 50 ml pure ethanol for 4 h. After this procedure, the obtained solution was placed on hotplate at a temperature of 80 °C for a full day. After drying, the samples were crushed again with a mortar to be ready for deposition.

2.2. Counter electrode fabrication

Drop-coating technique was employed to prepare the counter electrodes. In this method, slurry pastes of WO_3, ZCO and ZCO/WO_3 nanostructures was prepared; 60 mg precursor was added to 1.3 ml pure ethanol and dispersed by ultrasonic device. 100 μL of this solution was poured by a precise sampler onto FTO (1.5×1.5 cm^2). To control the geometry of the counter electrode, a special ribbon was used around the FTO. Then, the samples were heated up to a temperature of 50 °C on the hotplate to finish the dispositioning operation.

2.3. Photoanode preparation and DSSC assembling

Standard P25 TiO_2 was employed to fabricate the photoanodes. 100 mg P25 TiO_2 along with 120 mg ethyl cellulose ($C_{20}H_{38}O_{11}$) were dispersed in 5 ml pure ethanol and were vigorously stirred for 30 min at room temperature. Afterwards, the solution temperature was raised to 80 °C and the stirring continued for 60 min. At this step, 5 mg α-terpineol along with 5 drops of Triton X-100 were added to the solution and the stirring continued for 30 min. The prepared paste was deposited on FTO by doctor blade technique. Previously, The FTOs were covered with a blocking layer of dense TiO_2 to prevent electron recombination with electrolyte and dye molecules. After 15 min aging, the samples were put into an air furnace and sintered at 500 °C for 30 min. After cooling, the samples were soaked in 0.3 mM N179 dye (Dyesol Co., Australia) solution for 24 h at room temperature.

The solar cells were assembled by different counter electrodes. A Syrlin foil was used as a spacer, and the space between the two electrodes was filled with iodide-triiodide electrolyte (0.5 M lithium iodide (LiI), 0.05 M iodine (I_2), and 0.05 M *tert*-butyl pyridine dissolved in acetonitrile). Also, a control DSSC sample with a standard Pt counter electrode was prepared for comparison.

2.4. Characterization

To investigate the crystal structure of prepared nanostructures, XRD diffraction patterns were attained by STOE STADI-P X-ray diffractometer. In order to better examine the structure and chemical bonding of the synthesized samples, FTIR studies were performed by Bruker-Vector 22 in the range of 400–4000 cm^{-1}. The synthesized materials were mixed with KBr to form pellets. These pellets were placed inside the spectrometer and the transmission spectrum was measured. After extracting the FTIR data, the KBr spectrum was subtracted from the overall spectrum and the result was obtained in the form of a normalized curve. WITEC ALPHA300 RA-confocal Raman microscope with 532 nm excitation wavelength were used for structural and Raman analysis of synthesized samples. To inspect surface morphology of the synthesized counter electrodes, as well as the distribution of atomic elements, FESEM images and EDS analysis were prepared by Mira III Tescan field emission electron microscope with 15 kV operating voltage. A UV–Vis spectrophotometer (PerkinElmer Lambda 35) was used to determine the light absorption of the counter electrode samples. CV, Tafel, EIS, and Mott-Schottky electrochemical analyses were accomplished by potentiostat/galvanostat (EG&G model 273 A) in order to investigate the electrocatalytic activity and charge transfer properties of the manufactured samples. A 2450 Keithley source measure unit (SMU) with a solar simulator containing 350 W Xenon lamp equipped with AM1.5 filter (100 mW/cm^2) was employed for I–V tracing. The PVE300 photovoltaic QE system Bentham was used for IPCE analysis.

3. Results and discussion

Fig. 1 depicts the diffraction patterns for ZCO, WO_3 and ZCO/WO_3 samples. The peaks appearing for the ZCO sample at diffraction angles of 18.98, 31.33, 36.93, 38.52, 44.88, 55.64, 59.35 and 65.18°, respectively, represent the crystal planes (111), (220), (311), (222), (400), (422), (511) and (440) from the cubic phase of zinc cobalt oxide with Fd3m spatial symmetry. These peaks have a good coincidence with the standard card number 23-1390. According to the pattern, there are no additional phases and impurity in ZCO and the substance is single-phase. Moreover, by employing Debye-Scherrer equation [35];

$$D = \frac{k.\lambda}{\beta.\cos(\theta)}, \quad (1)$$

It is possible to estimate the crystallite size for this sample as an average of 28 nm. The sharpness of the peaks in the XRD patterns indicates the formation of larger crystals, which can be effective in the electron transport process to the surface of the counter electrode as well as its transfer to the electrolyte. The diffraction pattern of WO_3 sample shows peaks at angles of 23.30, 23.67, 24.27, 28.73, 33.33, 34.14, 35.62, 41.62, 47.21, 48.36, 49.80, 54.73, 55.76, 60.32, 62.36°, which are respectively associated with (001), (020), (200), (111), (021), (220), (121), (221), (002), (040), (140), (240), (420), (241) and (430) of the orthorhombic WO_3 with PE spatial symmetry (standard card number 20-1324). The observed peaks show the good purity of the sample and the absence of secondary phases, which guarantees the quality of the material. Also, by using the Debye-Scherrer relation, it can be shown that the size of the crystals in this sample is around 19 nm, which is less than the ZCO sample. The reason for this is the broadening of the peaks, which of course can lead to the smaller crystallite size. As can be seen in the top pattern of Fig. 1, the ZCO/WO_3 composite includes peaks that can be considered a combination of the peaks of the separate phases of ZCO and WO_3. It can be imagined with a proper approximation that the ZCO and WO_3 samples are well combined and have formed a hybrid structure. However, the reaction between ZCO and WO_3 has not caused the creation of a new phase of other substances, and we are only dealing with a composite of the two materials.

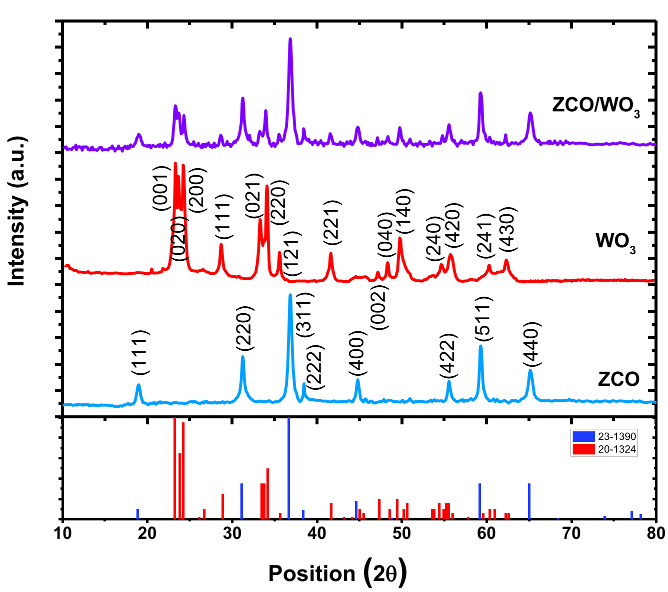

Fig. 1. XRD patterns for ZCO, WO_3 and ZCO/WO_3 synthesized nanostructures. At the bottom the XRD diffractions peaks are depicted for standard cards 23-1390 and 20-1324, which associated with ZCO and WO_3 materials, respectively.

The surface morphology of the synthesized counter electrodes is illustrated in Fig. 2. FESEM images acquired from ZCO, WO_3 and ZCO/WO_3 samples, correspondingly represent the surface structure of different counter electrodes in Fig. 2a, b and c. The morphology of ZCO is composed of nanoparticles include small pores. However, WO_3 consists of a more compact and uniform surface that does not have many pores. In Fig. 2c, the surface morphology of ZCO/WO_3 shows a composite state of ZCO nanoparticles and WO_3 nanostructures, which evokes a suitable involvement between ZCO and WO_3. This layer can provide the characteristics of ZCO and WO_3 at the same time. The distribution for atomic elements of ZCO/WO_3 sample can be realized in Fig. 2d along with EDS mapping for different elements O, Co, Zn and W. As can be seen, this layer is a combination of different elements with atomic percentages of 57, 19, 11 and 13% for O, Co, Zn and W elements, which has a small oxygen vacancy compared to the stoichiometric state. The atomic distribution and also the morphology of the ZCO/WO_3 counter electrode along with the XRD diffraction patterns indicate the formation of a suitable layer of ZCO and WO_3 combination, which can be used as an effective counter electrode in the DSSC.

In addition to the morphological and structural study of the synthesized samples, to inspect the formation of chemical bonding in the ZCO and WO_3 samples, FTIR spectra were prepared from them. Fig. 3a shows the FTIR spectra for the different counter electrodes. Both the samples have a broad peak in the range of 3000–3700 cm^{-1}, which indicates the stretching O–H bonds on the surfaces of the materials [36, 37]. The slight peaks can be observed at 1650 cm^{-1}, which specifies H–O–H bending modes and the physical presence of water at the surface [38]. The peaks are witnessed at 553 and 686 cm^{-1} in the ZCO sample represent the oscillation modes that related to Co–O and Zn–O bonding, respectively [39]. These two bonds can indicate the ZCO spinel phase in the counter electrodes [40]. Furthermore, in the WO_3 sample, the peaks appearing at 580 and 938 cm^{-1}, respectively characterize the oscillation modes of W–O and W=O, which justify the presence of WO_3 [41]. The W=O peak is usually formed when the substance is hydrated [42]. The sharpness of FTIR peaks, along with the reference to the mentioned chemical bonds, is conducive to the formation of high-quality and pure crystalline structures of ZCO and WO_3 materials, which are in good agreement with the XRD patterns.

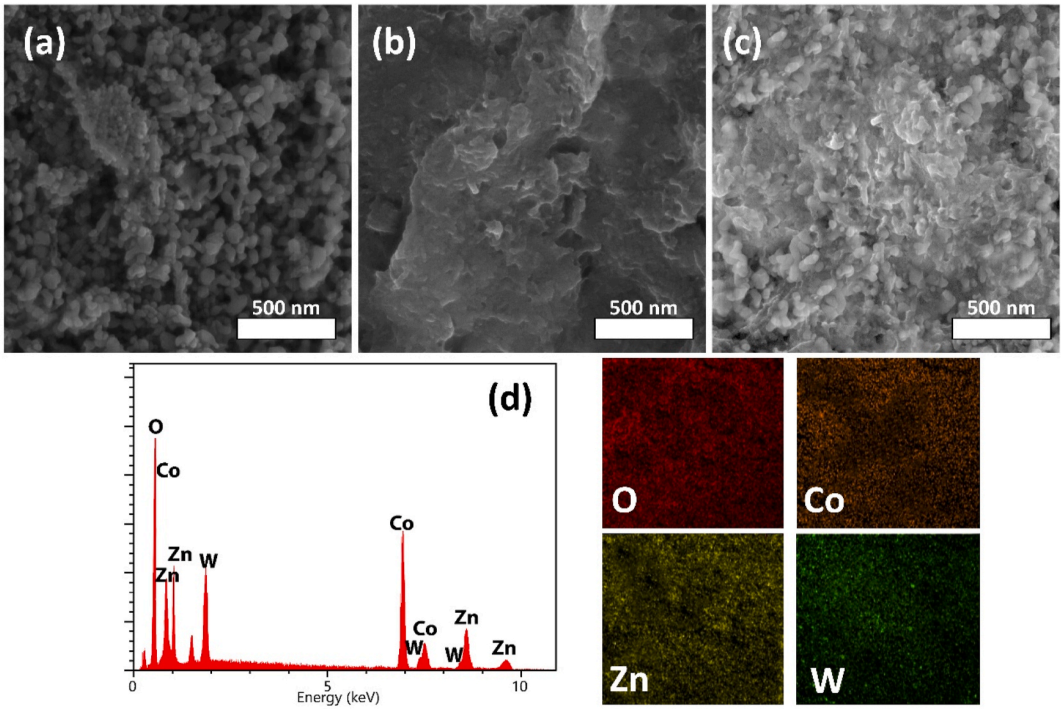

Fig. 2. FESEM images for (a) ZCO, (b) WO_3, and (c) ZCO/WO_3 samples. (d) The EDS atomic distribution and EDS mapping for the ZCO/WO_3 sample.

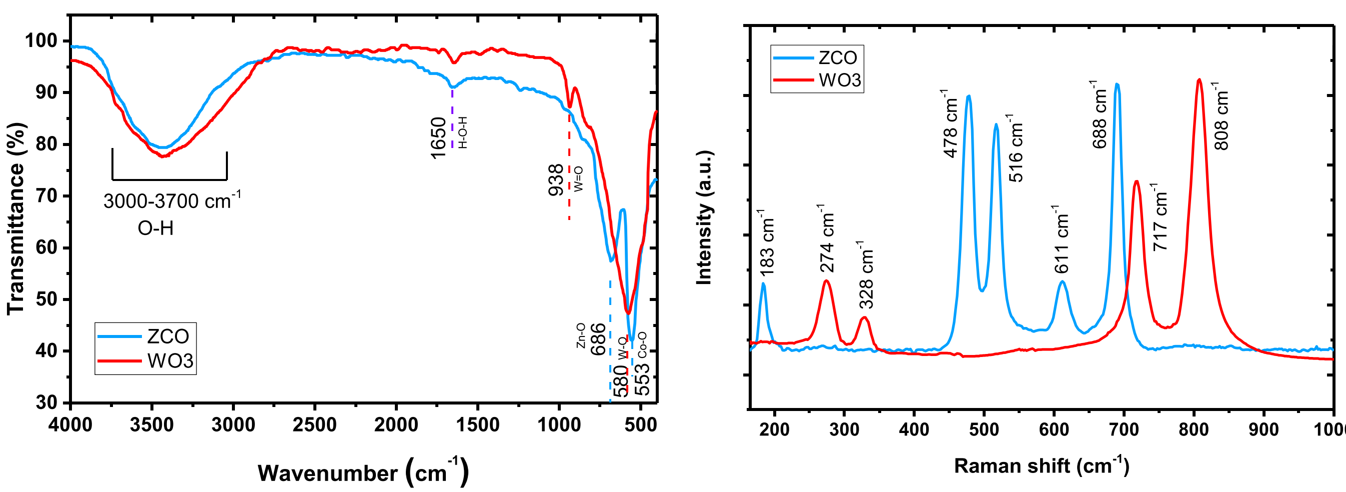

Fig. 3. (A) FTIR and (b) Raman spectrum for WO_3 and ZCO samples.

To further investigate the chemical bonds and structure of the synthesized samples, we used Raman analysis to complete the FTIR results. Fig. 3b shows the Raman spectra for the synthesized WO_3 and ZCO samples. As can be seen, the Raman peaks are very sharp, indicating the good crystalline quality of the synthesized samples. With more order of the crystal structure, the oscillating modes become more uniform and thus the peaks appear sharper. In WO_3 sample, four characteristic peaks are seen in the range of 200–1000 cm^{-1}. The prominent and sharp peaks appearing in 717 and 808 cm^{-1} are typical peaks of the WO_3 crystal structure, which usually represent the bridging oxygen stretching oscillations (O–W–O) [43]. In addition, two peaks at 274 and 328 cm^{-1} are related to W–O bending vibrations [44]. Furthermore, five sharp peaks can be recognized in the ZCO sample. The peaks appearing in wavenumbers 183, 516 and 611 cm^{-1} represent the F_{2g} phonon modes, which include Zn–O oscillations in the tetrahedral structure of the spinel ZCO [39]. The sharp peak of 688 is also related to Co–O stretching oscillations in the octahedral structure of ZCO [45]. The peak observed in 478 cm^{-1} represents the E_g phonon modes for the ZCO spinel structure [46].

Fig. 4a shows the absorption spectra in the UV and visible range for WO_3, ZCO and ZCO/WO_3 counter electrodes. WO_3 and ZCO counter electrodes have characteristic peaks in the range of 300 and 400 nm that distinguish them from each other. However, the absorption spectrum of the ZCO/WO_3 composite sample overlaps the two spectra of ZCO and WO_3, which indicates the combination of these two materials. The optical bandgap of the counter electrode samples can be measured according to the Tauc equation:

$$\alpha h\nu = A\left(h\nu - E_g\right)^n. \tag{2}$$

In this equation, α is the absorption coefficient, $h\nu$ denotes the photon energy, A is a constant, E_g represents the bandgap, and n is a constant number. $n = 1/2$ is used for direct semiconductors and $n = 2$ for indirect semiconductors. Fig. 4b shows the Tauc plots for the different synthesized counter electrodes. According to Tauc equation, when $\alpha h\nu = 0$, the

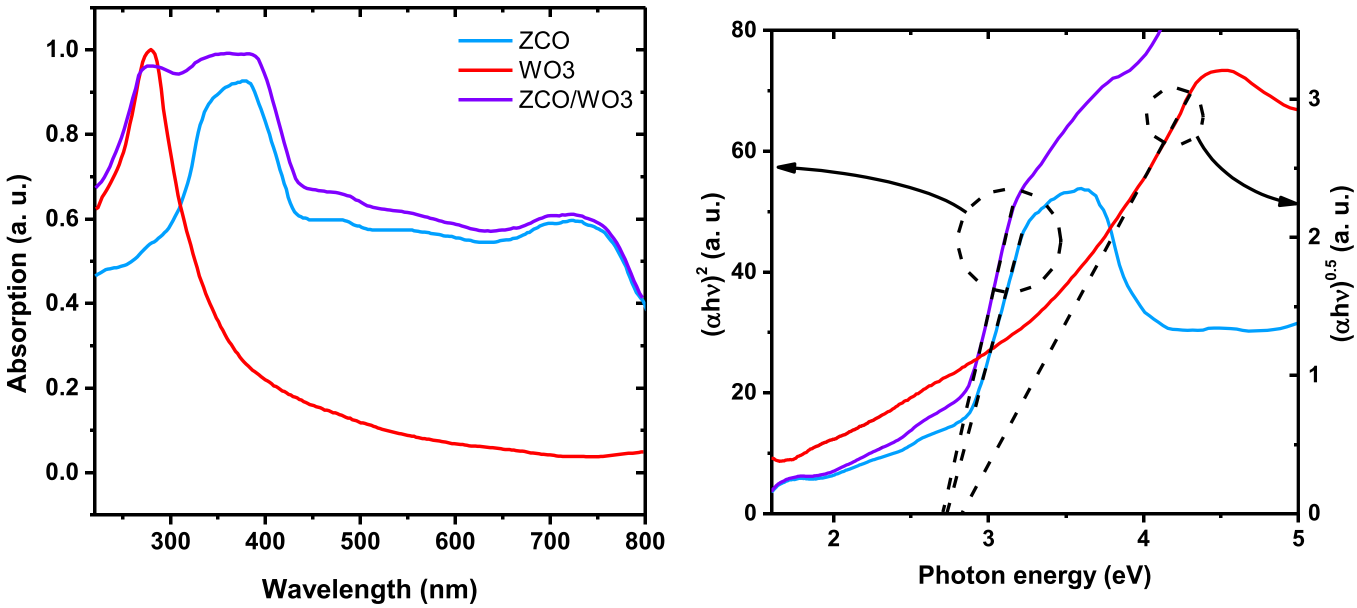

Fig. 4. (A) Absorption spectra, and (b) Tauc plots for different synthesized counter electrodes.

photon energy will be equal to the semiconductor bandgap. Therefore, it is possible to calculate the bandgap by fitting the linear part of the Tauc plots. It should be noted that WO_3 is considered as an indirect semiconductor, so its plot is drawn with $n = 2$. We have used $n = 1/2$ to draw the ZCO/WO_3 Tauc plot. Beside the fact ZCO is a direct semiconductor, higher percentage of the ZCO/WO_3 counter electrode is made of ZCO, and the indirect bandgap of WO_3 is less obvious in it. The optical bandgap for all three counter electrodes is almost close to each other and is in the range of 2.71–2.83 eV. These results have been previously mentioned in other researches [47,48].

In order to investigate the electrochemical properties of different counter electrodes and determine their electrocatalytic and transport properties, CV, Tafel, EIS, and Mott-Schottky analyses were prepared. Fig. 5a shows the CV curves for ZCO, WO_3, ZCO/WO_3 and standard Pt counter electrodes. In this analysis, a conventional 3-electrode electrochemical cell was used with WO_3, ZCO/WO_3, and Pt working electrode, Ag/AgCl reference electrode and a platinum wire as counter electrode. We also used the I^-/I_3^- electrolyte solution as the medium of redox reactions to illustrate the interactions occurred on the surface of the counter electrode in the DSSC. The applied potential performs in the range between −0.5 V and 1.5 V by the potentiostat with rate of 10 mV/s. As Fig. 5a shows, the CV curves consist two reduction and oxidation peaks, which represent the reactions $2I_2+2e^- \leftrightarrows 2I_3^-$ and $I_3^-+2e^- \leftrightarrows 2I^-$ [49]. In the DSSC mechanism under light irradiation, the electrolyte species reduction process occurs on the surface of the counter electrode, so the half-reaction $I_3^-+2e^-\rightarrow 2I^-$ is of special standing [50]. The faster and more intense the counter electrode can accomplish the reduction reaction, it actually provides more electrons for the regeneration the dye molecules and can increase the photocurrent. In this way, CV analysis can evaluate the electrocatalytic activity of the counter electrode with more current peak. In fact, with the increase of the peak related to $I_3^-+2e^-\rightarrow 2I^-$ reaction, the electrocatalytic activity of the counter electrode increases, and it indicates the better performance of the solar cell. As can be seen from Fig. 5a, the half-reaction peak in WO_3 sample shows the lowest value, which indicates its low electrocatalytic activity. The ZCO sample has a larger peak, however, compared to the Pt sample, it is still less active. Although both WO_3 and ZCO counter electrodes alone have inferior electrocatalytic activity compared to Pt, the ZCO/WO_3 composite sample demonstrates higher peak than Pt, and this indicates the enhanced electrocatalytic activity.

Tafel analysis was prepared to better evaluate the electrocatalytic activity of the synthesized counter electrodes. The semi-logarithmic plots of the anodic and cathodic current vs over-potential can be seen in Fig. 5b for different samples. The intersection of the diagrams in the Tafel zone with the $\eta = 0$ axis represents the exchange current (J_0), which can estimate the electrocatalytic activity of the layers [51]. The higher exchange current leads to the more electrocatalytic activity. As can be seen in the figure, the exchange current for the ZCO/WO_3 sample is higher than the ZCO, WO_3 and even Pt sample, which indicates its better performance.

To determine the charge transfer properties of different counter electrode, electrochemical impedance spectroscopy (EIS) was achieved. The results of this analysis can be seen as Nyquist plots in Fig. 5c. We used a symmetrical structure of CE/electrolyte/CE in the setup of this analysis, in which a pair of counter electrodes is immersed in the Na_2SO_4 electrolyte solution to eliminate the other effects. The frequency is modulated between 0.1 Hz and 20 kHz and a disturbance potential of 10 mV is introduced to the arrangement at each frequency point under dark condition and at room temperature. Normally, one semicircle should be appeared for each interface in Nyquist plot [52]. However, in all samples, only one semicircle is realized, which is due to the symmetrical structure, since both the electrodes are selected as the same material. The diameter of the semicircles represents the charge transfer resistance at counter electrode/electrolyte interface [53]. Also, the real part of the impedance at high frequencies that produce the points on the left side of the Nyquist plot is known as the series resistance (R_S). This resistance is caused by the contact resistance, the series resistance of the solution and the FTO. As it is clear from Fig. 5c, the R_S for all the samples is in the same range of 10–39 $\Omega\ cm^2$. The series resistance of the Pt sample is the lowest due to the better conductivity of the sample. The charge transfer resistance (R_{CT}) for WO_3, ZCO, ZCO/WO_3 and Pt samples is 565, 450, 235 and 357 $\Omega\ cm^2$, respectively. As it is realized, the pure WO_3 and ZCO samples show higher charge transfer resistance than Pt, but the charge transfer resistance for the composite ZCO/WO_3 electrode is significantly lower than that of Pt sample.

Lastly, to better investigate the electronic properties of the synthesized counter electrodes, we prepared Mott-Schottky analysis from them. The curves in Fig. 5(d–f) show the $1/C^2$ in terms of applied potential for WO_3, ZCO and ZCO/WO_3 counter electrodes. As can be seen, the slope of $1/C^2$ curve in Fig. 5d related to WO_3 is positive, which indicates that this counter electrode is n-type semiconductor. WO_3 is considered an intrinsically n-type semiconductor, which usually arises

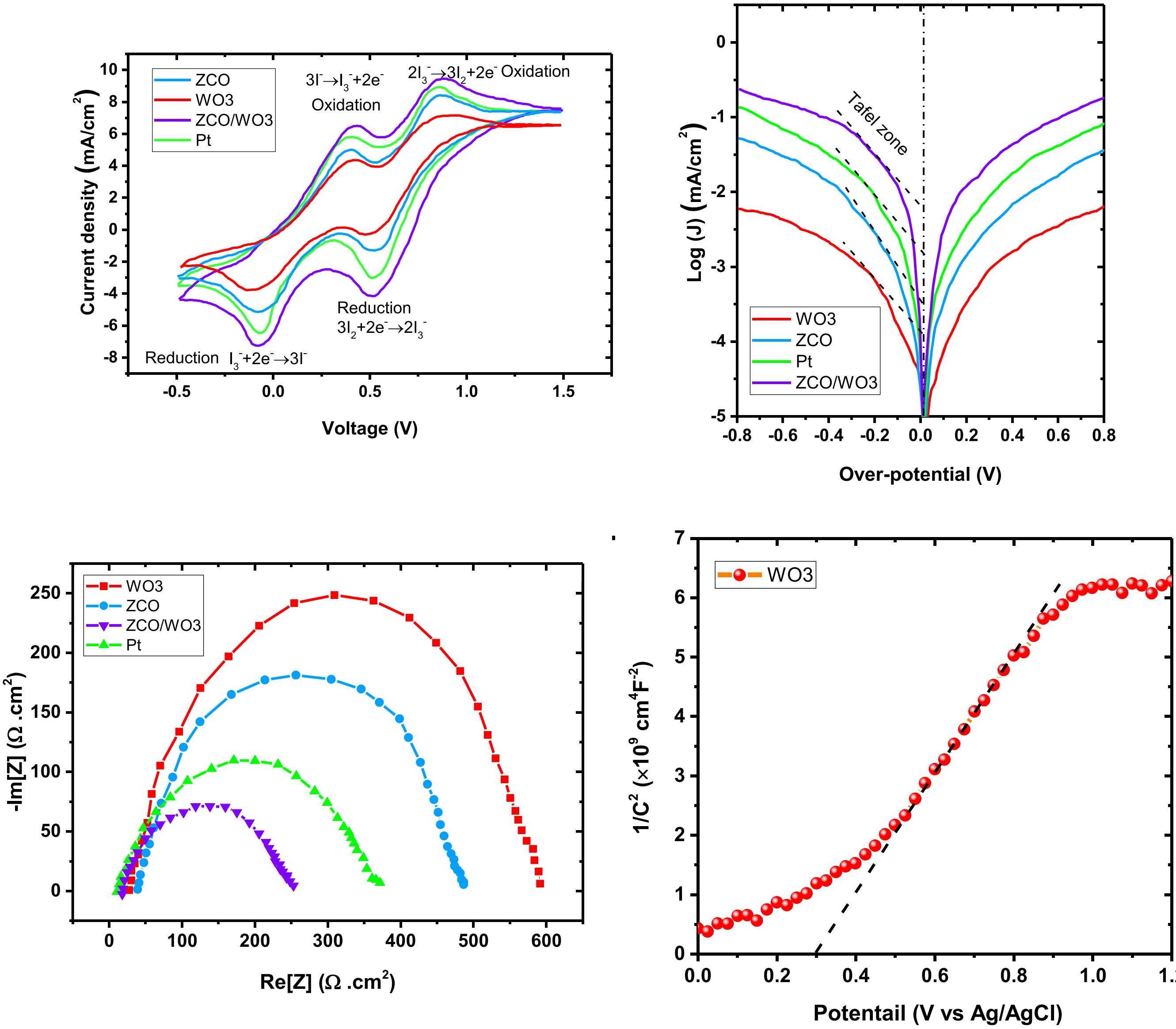

Fig. 5. (A) CV curves, (b) Tafel diagrams, (c) Nyquist plots, (d–f) Mott-Schottky analyses for different counter electrodes.

from oxygen vacancy defects [54]. Contrariwise, the $1/C^2$ curve slope for the ZCO counter electrode is negative, which means that this semiconductor is p-type semiconductor. ZCO usually possess natural defects such as Zn_{Co} antisite, which are known to be the main source of p-type conductivity in this material [55]. The Mott-Schottky curve of the composite ZCO/WO_3 sample includes an inverted V-shape feature, which is reminiscent of a p-n junction. This behavior has also been observed before in p-n junctions [56]. In fact, the combination of p-type ZCO and n-type WO_3 produces a kind of p-n junction, which can even contribute to the better performance of the DSSC [30]. The charge separation in the counter electrode makes their transport more efficient. The carrier density can be approximated using the Mott-Schottky equation:

$$\frac{A^2}{C^2} = \frac{2}{\varepsilon\varepsilon_0 q N_d}\left(V - V_{FB} - \frac{k_b T}{e}\right). \tag{3}$$

In this equation, C is the space charge capacity in the semiconductor, A stands for the surface area of the counter electrode, q is the elementary charge, N_d is carrier concentration, $\varepsilon\varepsilon_0$ represents the semiconductor permittivity, V and V_{FB} are the applied and flat band potentials, k is Boltzmann's constant, and T is absolute temperature. The carrier density can be obtained by calculating the slope of the curves in Fig. 5d-f. For WO_3 counter electrode, the carrier density is approximately 2.86×10^{18} cm^{-3}, while the carrier density for the ZCO sample is estimated to be 9.14×10^{17} cm^{-3}. The carrier density in the ZCO/WO_3 composite sample is similarly estimated by calculating two slopes in the linear region, which has a slight change compared to the single WO_3 and ZCO samples. In ZCO or WO_3 counter electrodes, holes or electrons must travel through the nanostructure semiconductor and react with electrolyte on the CE surface. While in the composite ZCO/WO_3 CE, electrons and holes are separated faster, allowing electrons to proceed on the path with minimal recombination. Likewise, decreased recombination improved the charge transfer process at the CE/electrolyte interface, enhancing electrocatalytic activity [30]. In the semiconductor science

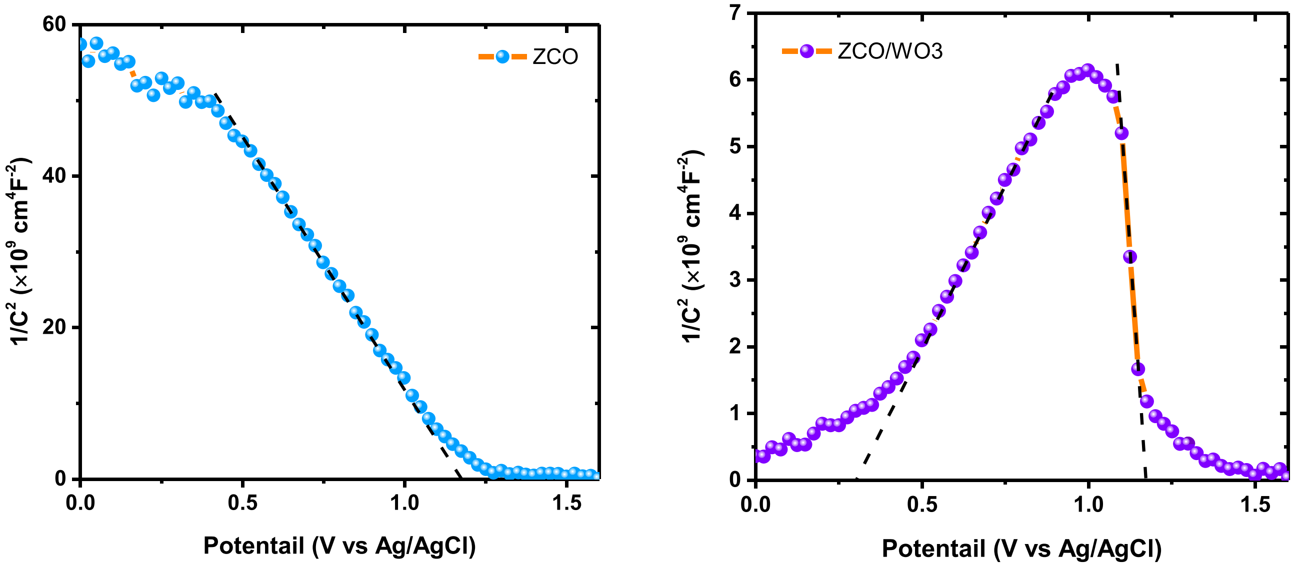

Fig. 5. (*continued*).

point of view, the holes that travel from the electrolyte to the CE can be injected into the CE and delivered into the circuit more easily.

The electrocatalytic activity of the ZCO/WO_3 counter electrode is much higher than that of the pure ZCO and WO_3 ones. This hybrid counter electrode has even better activity than the Pt sample. All four imperative CV, Tafel, EIS, and Mott-Schottky analyzes confirm the fact that this compound can improve the electrocatalytic properties. Moreover, the electrocatalytic activity trends have been well repeated in all the analyses, which validate the effectiveness of the composite structure. The reason for the improvement of electrocatalytic activity can be explained as follows; WO_3 layers have good transport properties due to their almost dense and uniform structure, but they do not have much porosity to have more contact surface with the electrolyte. On the contrary, the ZCO sample has a higher effective surface and can be effective in interacting with the electrolyte. However, both individual WO_3 and ZCO samples do not have much chance to compete with the Pt counter electrode. The ZCO/WO_3 layer, on the other hand, includes the porous part of ZCO due to nanoparticles and also benefits from the good charge transport properties of WO_3. In this sense, similar to hierarchical structures, ZCO nanoparticles are responsible for exchanging electrons with the electrolyte, and WO_3 material is responsible for transporting them. Therefore, its electrochemical properties are greatly enhanced.

After the investigating the structural and electrochemical properties of different counter electrodes, the solar cells were characterized with assembled DSSCs based on various counter electrodes and TiO_2 photoanode. The results of their current-voltage characteristic curves can be seen in Fig. 6a. Also, the photovoltaic parameters are tabulated in Table 1. The DSSC assembled by ZCO/WO_3 counter electrode having open circuit voltage (V_{OC}) of 691 mV, short circuit current (J_{SC}) of 17.54 mA/cm^2 and filling factor (FF) of 64% shows the highest efficiency (PCE) of 7.76%. The Pt, ZCO, and WO_3 DSSCs rank next with efficiencies of 7.26, 5.57, and 3.25%, respectively. Considering the results and the

Table 1
Photovoltaic parameters for DSSCs fabricated by different counter electrodes extracted from I–V curves.

Solar cell	V_{OC} (mV)	J_{SC} (mA/cm^2)	FF (%)	PCE (%)
WO_3	591 ± 9	8.89 ± 0.08	62 ± 0.7	3.26 ± 0.08
ZCO	647 ± 26	13.88 ± 0.07	62 ± 0.7	5.57 ± 0.19
ZCO/WO_3	691 ± 5	17.54 ± 0.10	64 ± 0.8	7.76 ± 0.09
Pt	683 ± 3	16.87 ± 0.06	63 ± 0.7	7.26 ± 0.11

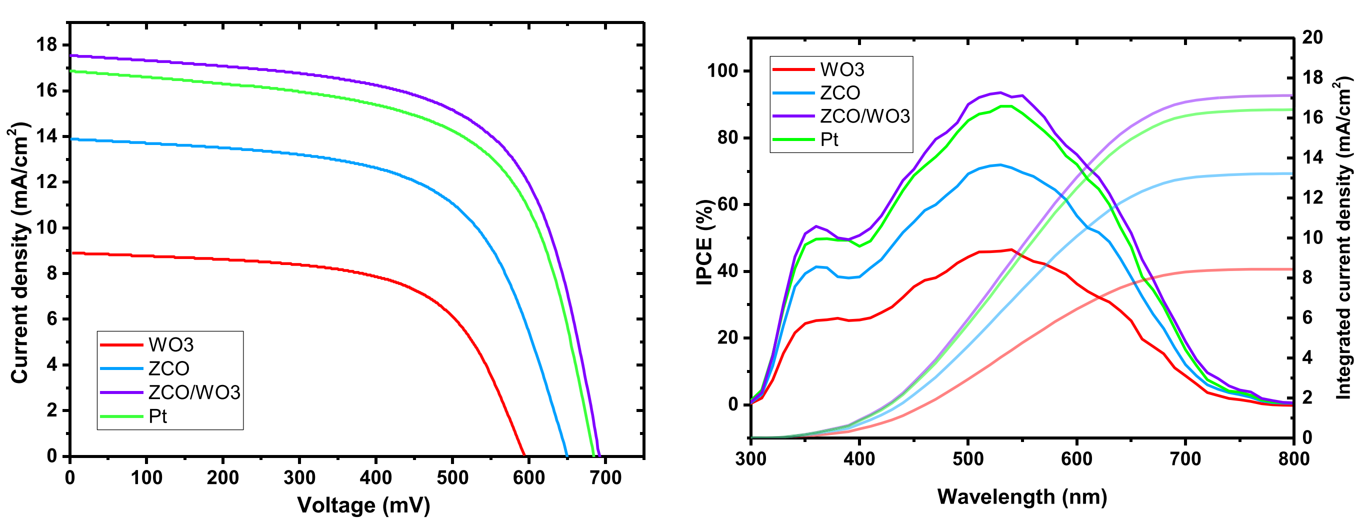

Fig. 6. (A) J-V characteristics, and (b) IPCE curves for different solar cells assembled with WO_3, ZCO, ZCO/WO_3, and Pt counter electrodes.

fact that the photoanodes are all the same, one can comprehend the fact that the effect of the counter electrode is impressive. The DSSC based on the ZCO/WO_3 counter electrode with the best electrocatalytic activity shows the highest efficiency. The significant effect of the counter electrode is mostly to increase the short circuit current. In actual fact, the ZCO/WO_3 counter electrode supplies electrons to the electrolyte with higher speed and intensity, so, the current passing through the cell increases. Furthermore, a slight improvement in FF and V_{OC} is observed, which can also be attributed to the better activity of the counter electrode. The ZCO/WO_3 counter electrode has significantly improved the solar cell performance compared to the pure samples by having better charge transport and transfer properties than the separate ZCO and WO_3 samples.

Fig. 6b shows the incident photon-to-current efficiency (IPCE) curves for different solar cells based on different counter electrodes in the range of 300–800 nm. The ZCO/WO_3 sample demonstrates a higher IPCE in all wavelengths than its competitors. In the range of 470–580 nm, where the IPCE diagram reaches its maximum value due to the absorption region of the N719 molecule [57], the ZCO/WO_3 solar cell has a quantum efficiency between 80 and 90%, which is 3–5% higher than that of the Pt electrode. This means the short circuit current for the ZCO/WO_3 sample is higher than that of the Pt sample and other samples. In addition, the integrated current density plots are depicted in Fig. 6b, using the equation:

$$J_{sc} = \int_{\lambda_1}^{\lambda_2} q.\Phi_{Ph}(\lambda).\text{IPCE}(\lambda)\, d\lambda \quad (4)$$

In this equation, λ_1 and λ_2 are the initial and final wavelengths of the spectrum, $\Phi_{Ph}(\lambda)$ is the photon flux of AM1.5 spectrum, and q is the electron charge. The short circuit current obtained from the above equation and IPCE diagram for WO_3, ZCO, ZCO/WO_3 and Pt samples is equal to 8.43, 13.22, 17.15 and 16.41 mA/cm^2, respectively. As can be seen, there is a good agreement between the short-circuit current extracted from the IPCE analysis and the J-V characteristic curve that previously observed.

Fig. 7 shows the Box and Whisker plots of the photovoltaic parameters for 60 DSSCs assembled with different counter electrodes. To examine the accurateness of the results and their reproducibility, we prepared 15 similar DSSC from each counter electrode sample. According to Fig. 7, the reproducibility of the results can be evaluated favorably. The PCE standard deviation in WO_3, ZCO, ZCO/WO_3 and Pt samples is estimated to be 0.08, 0.19, 0.09, and 0.11%, respectively. It can be seen that by repeating the characterization of different DSSCs, almost the same results are obtained in each case.

4. Conclusion

In this research, we fabricated $ZnCo_2O_4$ (ZCO), WO_3 and ZCO/WO_3 layers using combustion, sol-gel and solid-state reaction methods and employed them as counter electrodes in DSSC structure. Examining the structural, morphological, and optical properties of the ZCO/WO_3 sample shows that this layer is a composite of ZCO and WO_3. Also, the investigation on the electrochemical properties shows that the electrocatalytic activity of the counter electrodes is improved by the formation of the composite. The CV, Tafel, EIS, and Mott-Schottky analyses confirm that the charge transfer properties and electrocatalytic activity of the ZCO/WO_3 sample are enhanced compared to their pure samples. The increase in electrocatalytic activity can be attributed to the hierarchical structure and taking advantage of the unique properties of ZCO/WO_3 components. In this way, the charge transport and transfer properties were improved by the structures of WO_3 and ZCO nanoparticles in the ZCO/WO_3 counter electrode. Also, the DSSC based on ZCO/WO_3 counter electrode attained the highest efficiency among all the other

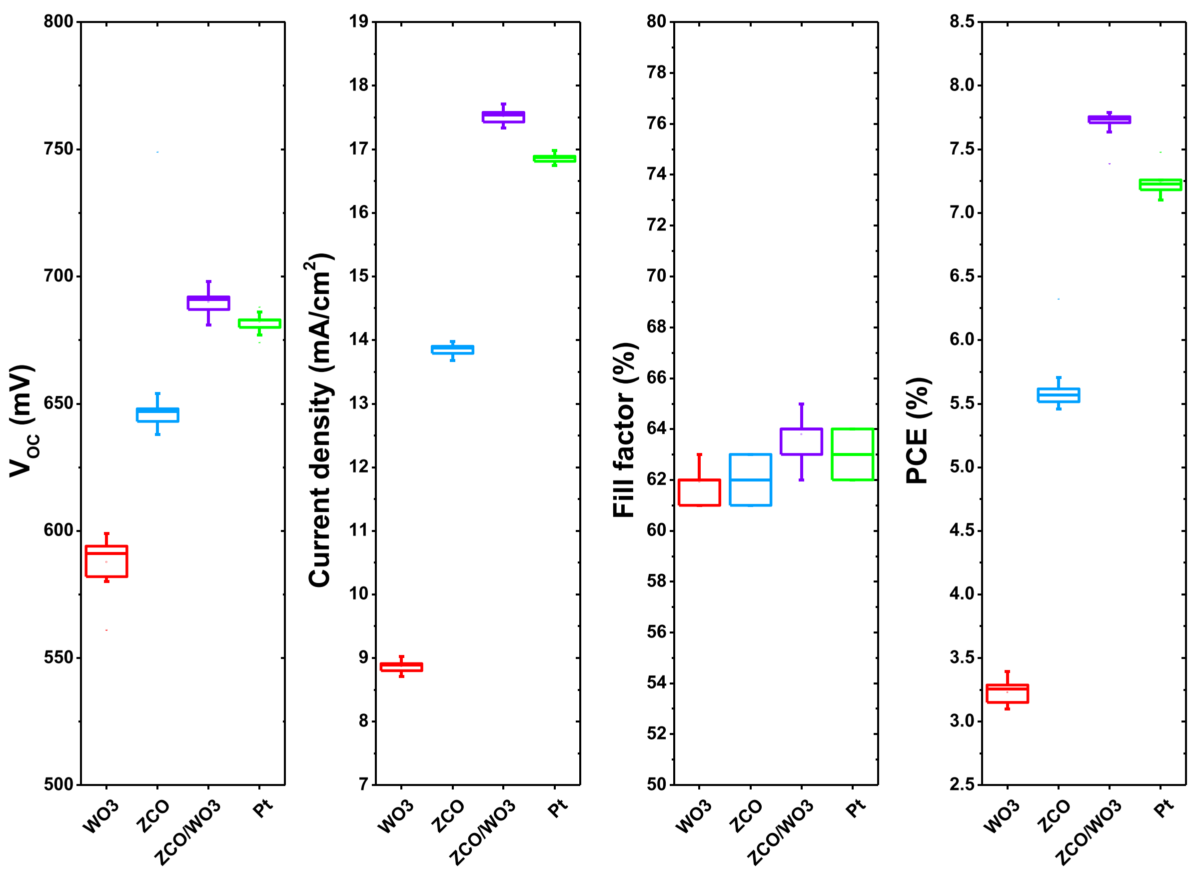

Fig. 7. Box and Whisker plots for photovoltaic parameters achieved from 60 DSSCs.

competitors by obtaining an efficiency of 7.76%, which can promise to get rid of expensive Pt counter electrodes.

Declarations

No funding was received to assist with the preparation of this manuscript.

The authors have no relevant financial or non-financial interests to disclose.

CRediT authorship contribution statement

Raed H. Althomali: Methodology, Writing – original draft, Formal analysis. **Ebraheem Abdu Musad Saleh:** Formal analysis, Investigation, review & editing. **Ramesh S. Bhat:** Project administration, Conceptualization, review & editing. **Shavan Askar:** Formal analysis, Investigation, review & editing. **I.B. Sapaev:** Formal analysis, Investigation, review & editing. **Mazin A.A. Najm:** Formal analysis, Investigation, review & editing. **Benien M. Ridha:** Visualization, Data curation, review & editing. **Ali H. Alsalamy:** Visualization, Data curation, review & editing. **Russual Riyadh:** Validation, Data curation, review & editing.

Declaration of competing interest

The authors declare that they have no known competing financial interests or personal relationships that could have appeared to influence the work reported in this paper.

Data availability

Data will be made available on request.

References

[1] B. O'Regan, M. Grätzel, A low-cost, high-efficiency solar cell based on dye-sensitized colloidal TiO2 films, Nature 353 (1991) 737–740.
[2] F. Mujtahid, P.L. Gareso, B. Armynah, D. Tahir, Review effect of various types of dyes and structures in supporting performance of dye-sensitized solar cell TiO2-based nanocomposites, Int. J. Energy Res. 46 (2022) 726–742.
[3] D. Devadiga, M. Selvakumar, P. Shetty, M.S. Santosh, Dye-sensitized solar cell for indoor applications: a mini-review, J. Electron. Mater. 50 (2021) 3187–3206.
[4] M. Abrari, M. Ahmadi, M. Ghanaatshoar, H.R. Moazami, S.S.H. Davarani, Fabrication of dye-sensitized solar cells based on SnO2/ZnO composite nanostructures: a new facile method using dual anodic dissolution, J. Alloys Compd. 784 (2019) 1036–1046.
[5] Y. Kumar, T. Chhalodia, P.K.G. Bedi, P.L. Meena, Photoanode modified with nanostructures for efficiency enhancement in DSSC: a review, Carbon Lett. (2022).
[6] K. Kakiage, H. Osada, Y. Aoyama, T. Yano, K. Oya, S. Iwamoto, J. Fujisawa, M. Hanaya, Achievement of over 1.4 V photovoltage in a dye-sensitized solar cell by the application of a silyl-anchor coumarin dye, Sci. Rep. 6 (2016), 35888.
[7] H. Michaels, M. Freitag, Assessment of TiO2 blocking layers for CuII/I-electrolyte dye-sensitized solar cells by electrochemical impedance spectroscopy, ACS Appl. Energy Mater. 5 (2022) 1933–1941.
[8] T. Kono, N. Masaki, M. Nishikawa, R. Tamura, H. Matsuzaki, M. Kimura, S. Mori, Interfacial charge transfer in dye-sensitized solar cells using SCN-free terpyridine-coordinated Ru complex dye and Co complex redox couples, ACS Appl. Mater. Interfaces 8 (2016) 16677–16683.
[9] Y. Liu, Y. Cao, W. Zhang, M. Stojanovic, M.I. Dar, P. Péchy, Y. Saygili, A. Hagfeldt, S.M. Zakeeruddin, M. Grätzel, Electron-affinity-triggered variations on the optical and electrical properties of dye molecules enabling highly efficient dye-sensitized solar cells, Angew. Chem., Int. Ed. 57 (2018) 14125–14128.
[10] A. Zatirostami, Electro-deposited SnSe on ITO: a low-cost and high-performance counter electrode for DSSCs, J. Alloys Compd. 844 (2020), 156151.
[11] A. Zatirostami, SnO2- based DSSC with SnSe counter electrode prepared by sputtering and selenization of Sn: effect of selenization temperature, Mater. Sci. Semicond. Process. 135 (2021), 106044.
[12] A. Zatirostami, Carbon black/SnSe composite: a low-cost, high performance counter electrode for dye sensitized solar cells, Thin Solid Films 725 (2021), 138642.
[13] M. Yang, G. Zhou, Y. Wei, Z. Huang, J. Zhang, Catalytic activity enhancement of Cu2ZnSnS4 due to composite of Co9S8 as counter electrode for dye-sensitized solar cells, J. Mater. Res. 37 (2022) 1835–1844.
[14] X. Yang, L. Zhou, A. Feng, H. Tang, H. Zhang, Z. Ding, Y. Ma, M. Wu, S. Jin, G. Li, Synthesis of nickel sulfides of different phases for counter electrodes in dye-sensitized solar cells by a solvothermal method with different solvents, J. Mater. Res. 29 (2014) 935–941.
[15] N. Narudin, P. Ekanayake, Y.W. Soon, H. Nakajima, C.M. Lim, Enhanced properties of low-cost carbon black-graphite counter electrode in DSSC by incorporating binders, Sol. Energy 225 (2021) 237–244.
[16] A.C.K. Reddy, M. Gurulakshmi, K. Susmitha, M. Raghavender, N. Thota, Y.P. V. Subbaiah, A novel PEDOT:PSS/SWCNH bilayer thin film counter electrode for efficient dye-sensitized solar cells, J. Mater. Sci. Mater. Electron. 31 (2020) 4752–4760.
[17] M.Ö. Karakuş, M.E. Yakışıklıer, A. Delibaş, E. Ayyıldız, H. Çetin, Anionic and cationic polymer-based quasi-solid-state dye-sensitized solar cell with poly(aniline) counter electrode, Sol. Energy 195 (2020) 565–572.
[18] Y. He, Z. Shen, G. Yue, Y. Gao, J. Huo, C. Dong, Y. Mao, F. Tan, A dye-sensitized solar cells with enhanced efficiency based on a "pillared effect" of CoMoP2 @Mxene@CNTs composite counter electrode, J. Alloys Compd. 922 (2022), 166279.
[19] M. Gao, Z. Shen, G. Yue, C. Dong, J. Wu, Y. Gao, F. Tan, One-pot hydrothermal in situ growth of In4SnS8@MoS2@CNTs as efficient Pt-free counter electrodes for dye-sensitized solar cells, J. Alloys Compd. 932 (2023), 167643.
[20] S. Elindjeane Sheela, V. Murugadoss, R. Sittaramane, S. Angaiah, Development of tungsten diselenide/polyaniline composite nanofibers as an efficient electrocatalytic counter electrode material for dye-sensitized solar cell, Sol. Energy 209 (2020) 538–546.
[21] L. Wei, Q. Wu, Y. Yang, B. Jiang, G. Sun, J. Feng, F. Yu, Y. Kang, G. Dong, One-step synthesis of nitrogen-decorated CeO2/reduced graphene oxide nanocomposite and its electrocatalytic activity for triiodide/iodide reduction, J. Mater. Res. 35 (2020) 1461–1471.
[22] W. Fu, Y. Wang, W. Han, Z. Zhang, H. Zha, E. Xie, Construction of hierarchical ZnCo2O4@NixCo2x(OH)6x core/shell nanowire arrays for high-performance supercapacitors, J. Mater. Chem. A 4 (2016) 173–182.
[23] T. Huang, C. Zhao, R. Zheng, Y. Zhang, Z. Hu, Facilely synthesized porous ZnCo2O4 rodlike nanostructure for high-rate supercapacitors, Ionics 21 (2015) 3109–3115.
[24] M. Ahmadi, M. Abrari, M. Ghanaatshoar, An all-sputtered photovoltaic ultraviolet photodetector based on Co-doped CuCrO2 and Al-doped ZnO heterojunction, Sci. Rep. 11 (2021).
[25] L. Xu, Y. Zhao, J. Lian, Y. Xu, J. Bao, J. Qiu, L. Xu, H. Xu, M. Hua, H. Li, Morphology controlled preparation of ZnCo2O4 nanostructures for asymmetric supercapacitor with ultrahigh energy density, Energy 123 (2017) 296–304.
[26] J. Theerthagiri, R.A. Senthil, A. Malathi, A. Selvi, J. Madhavan, M. Ashokkumar, Synthesis and characterization of a CuS–WO3 composite photocatalyst for enhanced visible light photocatalytic activity, RSC Adv. 5 (2015) 52718–52725.
[27] R. Gayathri, P. Rajeswaran, G. Raja, S.R. Bavaji, N. Ameen, M. Shkir, Fabrication of WO3 nanotubes/graphene oxide nanosheets hybrid structures: enhanced solar conversion efficiency in dye sensitized solar cell, Diam. Relat. Mater. 119 (2021), 108562.
[28] H. Hou, H. Shao, X. Zhang, G. Liu, S. Hussain, G. Qiao, RGO-loaded flower-like ZnCo2O4 nanohybrid as counter electrode for dye-sensitized solar cells, Mater. Lett. 225 (2018) 5–8.
[29] W. Wang, F. Du, Q. Yang, K. Zhang, J. Yao, G. Li, H. Zhou, Graphene-loaded porous ZnCo2O4 nanosheets composite as counter electrode for dye-sensitized solar cells, Mater. Lett. 207 (2017) 117–120.
[30] S.S. Abdullaev, Y. Fahad Breesam, A.A.H. AlZubaidi, A.K. Tripathi, A.K. Kareem, S. V. Kuznetsov, T. Alawsi, R.S. Zabibah, ZnO@ZnCo2O4 core-shell: a novel high electrocatalytic nanostructure to replace platinum as the counter electrode in dye-sensitized solar cells, Mater. Sci. Semicond. Process. 165 (2023), 107709.
[31] X. Zhang, X. Wang, Y. Cao, C. Liang, S. Geng, H. Guo, Y. Liu, Y. Luo, W. Zhang, L. Li, Facile synthesis of ZnCo2O4@NiMoO4 with porous coated structures on carbon paper as stable and efficient Pt-free counter electrode materials for advanced dye-sensitized solar cells, Appl. Surf. Sci. 616 (2023), 156461.
[32] P. Mahajan, R. Datt, V. Gupta, S. Arya, Synthesis and characterization of ZnO@ WO3 core/shell nanoparticles as counter electrode for dye-sensitized solar cell, Surface. Interfac. 30 (2022), 101920.
[33] Z. Shen, M. Wang, L. Liu, M.V. Sofianos, H. Yang, S. Wang, S. Liu, Carbon-coated three-dimensional WS2 film consisting of WO3@WS2 core-shell blocks and layered WS2 nanostructures as counter electrodes for efficient dye-sensitized solar cells, Electrochim. Acta 266 (2018) 130–138.
[34] W. Cui, J. Ma, K. Wu, J. Chen, mingxing Wu, The preparation and performance of WO3@C as a counter electrode catalyst for dye-sensitized solar cell, Int. J. Electrochem. Sci. 12 (2017) 11487–11495.
[35] M. Saeidi, M. Abrari, M. Ahmadi, Fabrication of dye-sensitized solar cell based on mixed tin and zinc oxide nanoparticles, Appl. Phys. A 125 (2019) 409.
[36] M. Abrari, M. Ghanaatshoar, S.S. Hosseiny Davarani, H.R. Moazami, I. Kazeminezhad, Synthesis of SnO$$_2$$2nanoparticles by electrooxidation of tin in quaternary ammonium salt for application in dye-sensitized solar cells, Appl. Phys. A 123 (2017) 326.
[37] S.S. Hosseiny Davarani, H.R. Moazami, T. Yousefi, M. Abrari, The flexible route for the electrosynthesis of visible light active CdxZn1-xOnanostructures by sequential anodic dissolution of metallic electrodes, J. Water Environ. Nanotechnol. 3 (2018) 235–242.
[38] M. Abrari, M. Ghanaatshoar, H.R. Moazami, S.S. Hosseiny Davarani, Synthesis of SnO2 nanoparticles by electrooxidation method and their application in dye-sensitized solar cells: the influence of the counterion, J. Electron. Mater. 48 (2019) 445–453.
[39] W. Wang, Facile hydrothermal synthesis of ZnCo2O4 nanostructures: controlled morphology and magnetic properties, J. Mater. Sci. Mater. Electron. 32 (2021) 16662–16668.

[40] X. Xiao, B. Peng, L. Cai, X. Zhang, S. Liu, Y. Wang, The high efficient catalytic properties for thermal decomposition of ammonium perchlorate using mesoporous ZnCo2O4 rods synthesized by oxalate co-precipitation method, Sci. Rep. 8 (2018) 7571.
[41] S. Bai, K. Zhang, J. Sun, D. Zhang, R. Luo, D. Li, C. Liu, Polythiophene-WO3 hybrid architectures for low-temperature H2S detection, Sens. Actuators, B 197 (2014) 142–148.
[42] S.N. Eroi, A.S. Ello, D. Diabaté, D.B. Ossonon, Heterogeneous WO3/H2O2 system for degradation of Indigo Carmin dye from aqueous solution, South Afr. J. Chem. Eng. 37 (2021) 53–60.
[43] P.S. Kolhe, P.S. Shirke, N. Maiti, M.A. More, K.M. Sonawane, Facile hydrothermal synthesis of WO3 nanoconifer thin film: multifunctional behavior for gas sensing and field emission applications, J. Inorg. Organomet. Polym. Mater. 29 (2019) 41–48.
[44] J. Díaz-Reyes, R. Castillo-Ojeda, M. Galván-Arellano, O. Zaca-Moran, Characterization of WO3 thin films grown on silicon by HFMOD, Adv. Condens. Matter Phys. 2013 (2013).
[45] V. Venkatachalam, A. Alsalme, A. Alswieleh, R. Jayavel, Double hydroxide mediated synthesis of nanostructured ZnCo2O4 as high performance electrode material for supercapacitor applications, Chem. Eng. J. 321 (2017) 474–483.
[46] A.J.C. Mary, A.C. Bose, Hydrothermal synthesis of Mn-doped ZnCo2O4 electrode material for high-performance supercapacitor, Appl. Surf. Sci. 425 (2017) 201–211.
[47] H. Guo, J. Chen, W. Weng, Q. Wang, S. Li, Facile template-free one-pot fabrication of ZnCo2O4 microspheres with enhanced photocatalytic activities under visible-light illumination, Chem. Eng. J. 239 (2014) 192–199.
[48] O. Samuel, M.H.D. Othman, R. Kamaludin, O. Sinsamphanh, H. Abdullah, M. H. Puteh, T.A. Kurniawan, WO3–based photocatalysts: a review on synthesis, performance enhancement and photocatalytic memory for environmental applications, Ceram. Int. 48 (2022) 5845–5875.
[49] M. Soltanmohammadi, V. Karimi, S. Alee, M. Abrari, M. Ahmadi, M. Ghanaatshoar, Cu2ZnSnS4 thin film as a counter electrode in zinc stannate-based dye-sensitized solar cells, Semicond. Sci. Technol. 36 (2021), 105008.
[50] Z. Jin, G. Zhao, Z.-S. Wang, Controllable growth of NixCoySe films and the influence of composition on the photovoltaic performance of quasi-solid-state dye-sensitized solar cells, J. Mater. Chem. C 6 (2018) 3901–3909.
[51] J. Wu, Z. Tang, Y. Huang, M. Huang, H. Yu, J. Lin, A dye-sensitized solar cell based on platinum nanotube counter electrode with efficiency of 9.05, J. Power Sources 257 (2014) 84–89.
[52] A. Moradi, M. Abrari, M. Ahmadi, Efficiency enhancement in dye-sensitized solar cells through the decoration of electro-spun TiO 2 nanofibers with Ag nanoparticles, J. Mater. Sci. Mater. Electron. 31 (2020) 16759–16768.
[53] M.J. Ju, I.T. Choi, M. Zhong, K. Lim, J. Ko, J. Mohin, M. Lamson, T. Kowalewski, K. Matyjaszewski, H.K. Kim, Copolymer-templated nitrogen-enriched nanocarbons as a low charge-transfer resistance and highly stable alternative to platinum cathodes in dye-sensitized solar cells, J. Mater. Chem. A 3 (2015) 4413–4419.
[54] Y. Yao, D. Sang, L. Zou, Q. Wang, C. Liu, A review on the properties and applications of WO3 nanostructure-based optical and electronic devices, Nanomaterials 11 (2021) 2136.
[55] H.-Y. Chen, P.-C. Chen, P-type spinel ZnCo2O4 thin films prepared using sol-gel process, Appl. Surf. Sci. 505 (2020), 144460.
[56] Y. Zhao, X. Huang, X. Tan, T. Yu, X. Li, L. Yang, S. Wang, Fabrication of BiOBr nanosheets@TiO2 nanobelts p–n junction photocatalysts for enhanced visible-light activity, Appl. Surf. Sci. 365 (2016) 209–217.
[57] R.H. Althomali, S.I.S. Al-Hawary, A. Gehlot, M.T. Qasim, B. Abdullaeva, I. B. Sapaev, I.H. Al-Kharsan, A. Alsalamy, A novel Pt-free counter electrode based on MoSe2 for cost effective dye-sensitized solar cells (DSSCs): effect of Ni doping, J. Phys. Chem. Solid. 182 (2023), 111597.